Experiments on a videotape atom chip: fragmentation and transport studies

I Llorente García, B Darquié‡, E A Curtis§, C D J Sinclair‖ and E A Hinds

Centre for Cold Matter, Department of Physics, Imperial College, Prince Consort Road, London SW7 2BW, UK.

E-mail: isabel.llorente-garcia@imperial.ac.uk

Abstract. This paper reports on experiments with ultra-cold rubidium atoms confined in microscopic magnetic traps created using a piece of periodically-magnetized videotape mounted on an atom chip. The roughness of the confining potential is studied with atomic clouds at temperatures of a few microKelvin and at distances between $30\,\mu$m and $80\,\mu$m from the videotape-chip surface. The inhomogeneities in the magnetic field created by the magnetized videotape close to the central region of the chip are characterized in this way. In addition, we demonstrate a novel transport mechanism whereby we convey cold atoms confined in arrays of videotape magnetic micro-traps over distances as large as $\sim 1\,$cm parallel to the chip surface. This conveying mechanism enables us to survey the surface of the chip and observe potential-roughness effects across different regions.

‡ Present address: Laboratoire de Physique des Lasers, CNRS UMR 7538, Université Paris 13, 99 avenue J.-B. Clément, 93430 Villetaneuse, France.
§ Present address: National Physical Laboratory, Hampton Road, Teddington, Middlesex TW11 0LW, UK.
‖ Present address: University College London Institute of Neurology, Queen Square, London WC1N 3BG, UK.

1. Introduction

The use of atom chips to trap neutral atoms and cool them down to temperatures of the order of 10^{-7} Kelvin has opened a wide range of possibilities for fundamental studies and applications requiring a high degree of control of an atomic system. An atom chip is a centimetre-scale device that integrates wires or permanent magnets (or both) in a flat geometry to generate the large magnetic field gradients required to confine neutral atoms at distances of the order of a few to a few hundred micrometres from the surface of the atom chip. Micro-fabricated magnetic traps for neutral atoms were first experimentally realized by J. Reichel *et al.* [1] in 1999, and by R. Folman *et al.* [2] in 2000, using surface-mounted wires on an atom chip. Atom chips offer the advantage of flexible trap configurations that range from single traps to arrays of multiple traps, as well as the possibility of integrating all elements necessary for trapping, cooling, transporting and detecting atoms into a single compact geometry.

Atom chips have been used for a wide variety of fundamental studies, for example: to investigate the behaviour of Bose-Einstein condensates as coherent matter waves in experiments such as atomic beam splitters or atomic interferometers [3–5]; to study low-dimensional quantum gases [6–10]; to explore atom-surface interactions [11–13], etc. Other applications of atom chips include for instance the use of ultra-cold atoms as magnetic field sensors [14–17] with high field sensitivity and high spatial resolution, and the experimental realisation of miniaturized atomic clocks [18, 19] which could be incorporated into Global Positioning Systems (GPS) and navigation systems. Atom chips also offer a promising experimental approach towards the implementation of quantum information processing with neutral atoms [20–22], since they can combine the accurate control of an atomic quantum system with coherent manipulation and integrated detection tools [23–30] in a miniaturized device with good prospects for scalability. More details can be found in the atom chip review of reference [31], and references therein.

The work described in this paper has been carried out with neutral ^{87}Rb atoms on a permanent-magnet atom chip made of videotape. Several cold-atom experiments around the world are working on atom chips based on different types of permanent magnets such as magnetic films [32, 33], planar structures of hard magnetic material [34–36], hard disk platters [37] or ferrimagnetic transparent films [38,39]. Magnetic data-storage media such as floppy disk, audiotape and videotape have been previously investigated in our group and used to manipulate ultra-cold atoms [40–45]. Several permanently-magnetized atom-chip designs have been investigated theoretically [46] as well as from a technical point of view [47].

The use of videotape to build an atom chip offers the advantage of miniaturized magnetic patterns that generate strong magnetic fields (up to $\sim 110\,\mathrm{G}$ at the chip surface) and strong field gradients (a few G/μm). The pattern of permanent magnetisation can be chosen according to the needs of the experiment. In our case, the recorded magnetisation is sinusoidal with a wavelength of $106\,\mu$m, allowing the confinement of

rubidium atoms with temperatures between a few hundred μK and a few hundred nK, in arrays of miniature magnetic micro-traps. An advantage of videotape is the fact that it is made of insulating material. This results in long trapping lifetimes, even close to the videotape [48], due to the low rate of thermally-induced spin flips compared to the rate near bulk metallic materials [13].

This paper begins by describing the videotape atom chip and the properties of the magnetic micro-traps in section 2, and continues in section 3 by detailing the experimental sequence followed to confine ultra-cold rubidium atoms in these traps. We then focus on two particular subjects. Section 4 describes a study of roughness of the trapping potential and fragmentation of atom clouds trapped in very close proximity to the surface of the atom chip. Section 5 describes an effective method of transporting cold atoms in videotape magnetic traps over large distances of the order of 1 cm, as a tool to increase the degree of control over the trapped atoms and to survey the surface of our videotape atom chip. More details about previous work on these two subjects are given at the beginning of sections 4 and 5.

2. The Chip

Design and fabrication of the videotape atom chip have been described in detail in our previous papers [48, 49]. A piece of commercial Ampex 398 Betacam SP videotape with dimensions of 22 mm $\times$ 12.5 mm, was glued onto a glass coverslip and coated with a 400 nm-thick reflective layer of gold. This was subsequently glued onto a block of stainless steel which houses auxiliary wires. Figure 1 shows a photograph of the chip together with a schematic view of the wires under the chip. The centre wire is used in an intermediate loading stage, together with a uniform bias field along x, to create a wire magnetic trap that transfers the atoms from a magneto-optical trap (MOT) into videotape magnetic micro-traps. The radio-frequency (rf)-antenna wires are used for evaporative cooling of the atoms in the magnetic traps and the end wires provide axial confinement. The overall diameter of the centre wire and rf-antenna wires is 0.5 mm, while that of the end wires is 1 mm. All wires are ceramic-coated copper conductors and can sustain currents of up to 20 A during times of up to 20 seconds.

The chip is mounted inside the chamber with its gold-coated face pointing downwards. The x, y and z directions shown in figure 1 are used throughout this paper. We establish here that y points down along the vertical direction, with $y = 0$ corresponding to the chip surface. The centre wire corresponds to the axis $x = 0$, $y = -440\,\mu$m, and the end wires are located at $y = -1.4\,$mm, $z = \pm 4\,$mm, with $z = 0$ corresponding to the centre of the chip, half way between the two end wires. Cold atoms are confined below the chip in elongated, tube-like traps, in such a way that z corresponds to the axial direction of the traps and x and y, to the transverse directions.

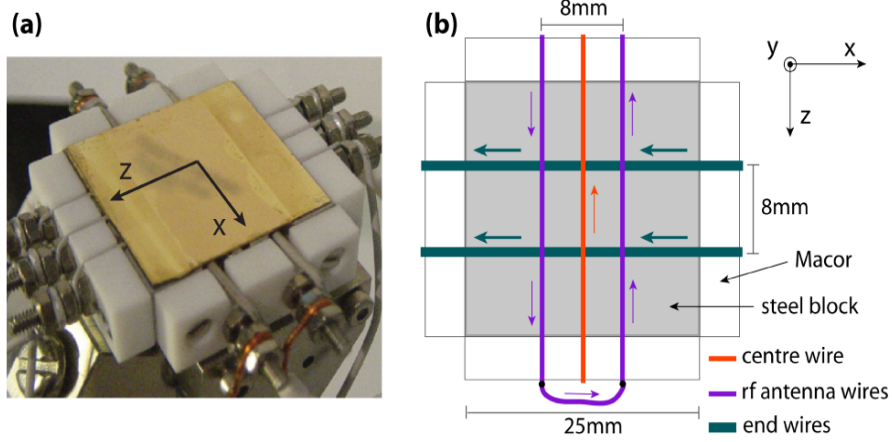The videotape is recorded with a periodic pattern of magnetisation, essentially

Figure 1. **(a)** Photograph of the videotape atom chip. **(b)** Schematic view of the wires under the chip. The arrows indicate the direction of the currents in the wires.

sinusoidal, given by $\vec{M} = M_1 \cos(kx)\hat{\mathbf{x}}$, where $k = 2\pi/\lambda$ and λ is the spatial period. A detailed calculation of the magnetic field generated by a periodically magnetized videotape can be found in reference [41]. Figure 2 shows an image of the videotape magnetisation seen by using a polarisation microscope, with a GGG (Gadolinium Gallium Garnet) magneto-optical sensor [50] placed on top of a videotape sample. This image is used to measure the period of the recorded pattern, $\lambda = (106.5 \pm 0.4)\,\mu m$ [51].
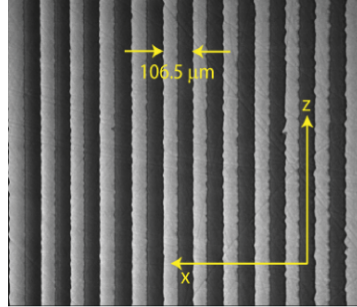

Figure 2. Image of the videotape magnetisation pattern acquired with a polarisation microscope and a magneto-optical garnet sensor. Note that the noise on the edges of the lines along the z direction is due to inhomogeneities in the garnet sensor: displacing the sensor along a fixed spot on the videotape changes the shape of this noise.

The videotape magnetisation generates a periodic magnetic field:

$$\vec{B}_{video} = B_1 e^{-ky} \left(- \cos(kx)\,\hat{\mathbf{x}} + \sin(kx)\,\hat{\mathbf{y}} \right) , \tag{2.1}$$

with

$$B_1 = \frac{\mu_0 M_1}{2}(1 - e^{-kb}) , \tag{2.2}$$

where μ_0 is the free-space magnetic permeability and b is the thickness of the magnetized layer in the videotape. The field strength, B_1, at the videotape surface is $B_1 =$

$(110 \pm 10)\,\mathrm{G}$ [49]. Equation (2.1) shows how the videotape field strength decreases exponentially with the distance from the surface. Moving along the x coordinate, the field direction rotates while its modulus remains constant. The corresponding videotape magnetic field lines are shown in figure 3 (a).
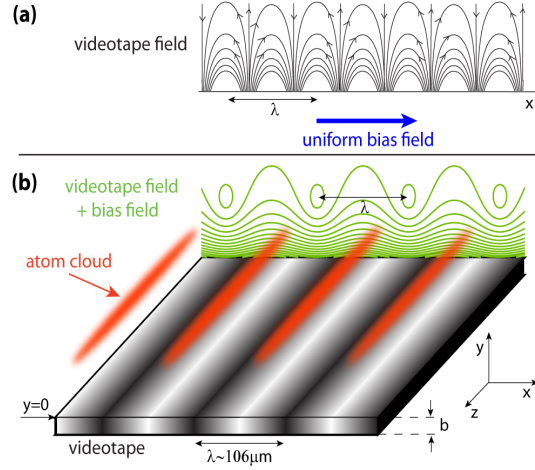

Figure 3. Magnetic fields used to create an array of videotape magnetic micro-traps. **(a)** Field lines generated by the sinusoidally magnetized videotape. **(b)** Contours of constant magnetic field strength of combined videotape field and bias field. As a result, atoms can be trapped in an array of elongated magnetic traps separated by a distance λ along x.

When a uniform bias field, $\vec{B}_b = B_b\hat{\mathbf{x}}$, is added along x, an array of magnetic micro-guides forms at a distance y_0 from the chip surface. This is the height at which the bias field cancels the videotape magnetic field:

$$y_0 = -\frac{1}{k}\ln\left(\frac{B_b}{B_1}\right). \tag{2.3}$$

Typical values of y_0 range between $20\,\mu\mathrm{m}$ and $120\,\mu\mathrm{m}$. The micro-guides in the array have their axes along z and are spaced along x by a distance $\lambda \sim 106\,\mu\mathrm{m}$. Figure 3 (b) shows the contours of constant magnetic field strength that result from combining the videotape field and bias field. Ultra-cold atoms are confined in lines along z, at the centre of each closed contour.

Axial confinement is provided by the magnetic field of the two end wires (figure 1). This is of the form $\vec{B}_{ew}(y,z) = B_{y-ew}(y,z)\hat{\mathbf{y}} + B_{z-ew}(y,z)\hat{\mathbf{z}}$. The components B_{y-ew} and B_{z-ew}, evaluated at a height $y = 40\,\mu\mathrm{m}$, are plotted in figure 4 as a function of the axial coordinate of the trap, z. Typically, a current $I_{end} = 10 - 15\,\mathrm{A}$ is run through the end wires, leading to axial trap frequencies of $12 - 15\,\mathrm{Hz}$ at distances up to a few hundred $\mu\mathrm{m}$ from the chip surface.

Helmholtz coils outside the chamber create an additional uniform field along z, referred to as B_{z-coil} throughout this paper, which reduces the magnitude of the net field ($B_z = B_{z-ew} - B_{z-coil}$) on the axis of the trap.
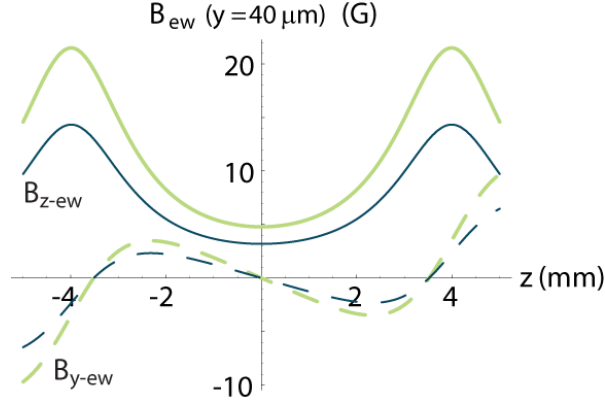
Figure 4. Z-component (solid lines) and y-component (dashed lines) of the end-wire field at a height $y = 40\,\mu\mathrm{m}$, as a function of z. The end wires are located at $z = \pm 4\,\mathrm{mm}$ and $y_0 = -1.4\,\mathrm{mm}$. Dark blue lines correspond to a current $I_{end} = 10\,\mathrm{A}$, and light green lines to $I_{end} = 15\,\mathrm{A}$.

Close to the central region of the trap, the frequency of small transverse oscillations of the atoms can be expressed as:

$$f_r \approx \frac{kB_b}{2\pi}\sqrt{\frac{\mu_B g_F m_F}{mB_z}} = \frac{kB_b}{2\pi}\sqrt{\frac{\mu}{mB_z}}, \tag{2.4}$$

where m is the mass of the atom and $\mu_B g_F m_F$ is the usual factor in the Zeeman energy, which we henceforth abbreviate to μ. The typical transverse oscillation frequencies in the videotape traps range from $500\,\mathrm{Hz}$ to $15\,\mathrm{kHz}$ for bias fields up to $40\,\mathrm{G}$.

It is possible, by modifying the bias field, the end-wire current and the magnitude of B_{z-coil}, to achieve independent control of all the relevant videotape trap parameters, i.e., the distance to the chip surface, the transverse trap frequencies, and the axial trap depth and frequency.

Figure 5 plots the modulus of the total magnetic field, as a function of each coordinate, for typical experimental parameters: $I_{end} = 15\,\mathrm{A}$, $B_b = 10.6\,\mathrm{G}$ and $B_{z-coil} = 2.6\,\mathrm{G}$, which result in a trap-surface separation $y_0 \sim 40\,\mu\mathrm{m}$. The top plots show $|\vec{B}|$ as a function of x, at $y = y_0$ and $z = 0$: the plot on the left-hand side shows how the periodic potential forms an array of micro-traps separated by $\lambda \sim 106\,\mu\mathrm{m}$ along x, while the plot on the right zooms into a single micro-trap. The bottom plots show the dependence of the confining field strength on y (left), evaluating $|\vec{B}|$ at $x = 0$ and $z = 0$, and on z (right), evaluating $|\vec{B}|$ at $x = 0$ and $y = y_0$. Note how the length scale along z is some two orders of magnitude larger than that along x or y. Thus, the traps are very elongated, with their axis along z, and can have aspect ratios up to 1000. The plots also show how the confinement is harmonic only in a limited region close to the centre of the traps.

Note that the addition of the end-wire field causes the height of the videotape traps to differ slightly (by $< 1\mu\mathrm{m}$) from the expression in equation (2.3) (because B_{z-ew} depends on y). Furthermore, B_{y-ew} causes the line of minimum magnetic field strength
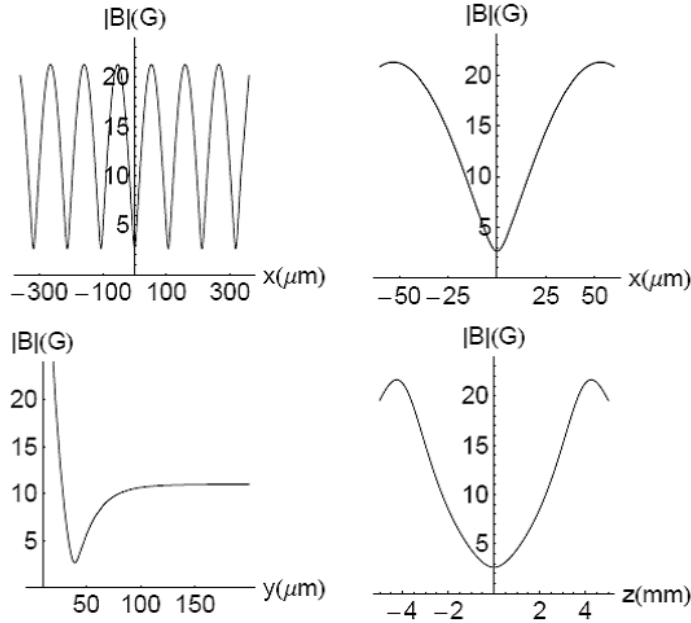
Figure 5. Total magnetic field strength in the videotape magnetic traps as a function of the x, y, z coordinates (see text for details), for $I_{end} = 15\,\mathrm{A}$, $B_b = 10.6\,\mathrm{G}$ and $B_{z-coil} = 2.6\,\mathrm{G}$. The trap height is $y_0 \sim 40\,\mu\mathrm{m}$.

of the traps, i.e., the effective trap axis, to be curved in three dimensions, instead of being a straight line parallel to z. These effects will be discussed in more detail in section 5.1. As a consequence, the transverse trap frequency slightly differs from that in equation (2.4), the principal axes of the trap deviate slightly from the x, y and z axes, and thus figure 5 does not rigorously represent the exact videotape trap cross-sections.

3. The experimental sequence

The experimental sequence that leads to optimum loading of cold atoms into videotape magnetic micro-traps is described here.

A two-chamber set up is used in which a slow beam of atoms ($\leq 10\,\mathrm{m/s}$) from a low-velocity intense source (LVIS) [52] loads a reflection MOT at the centre of the main chamber. A rubidium dispenser is turned on for $30\,\mathrm{s}$ and 10^8-10^9 atoms are captured in the MOT at a distance of $6 - 7\,\mathrm{mm}$ from the videotape-chip surface. The MOT temperature is a few hundred μK, its density around $10^9 - 10^{10}\,\mathrm{atoms/cm^3}$, and its lifetime, $50 - 160\,\mathrm{s}$. The MOT is then moved over $100\,\mathrm{ms}$ to a position $2\,\mathrm{mm}$ away from the chip surface by ramping up an external bias field of $3.6\,\mathrm{G}$ on the x-y plane. At this point, the red-detuning of the MOT beams is increased from $-12\,\mathrm{MHz}$ to $-45\,\mathrm{MHz}$ over $5\,\mathrm{ms}$ and held for another $5\,\mathrm{ms}$, in order to reduce the temperature of the atoms to $30 - 60\,\mu\mathrm{K}$ in a sub-Doppler cooling stage. The trapping light and quadrupole field of the MOT are then switched off and a $3.7\,\mathrm{G}$ field is turned on along the z direction to act as quantisation axis during an optical pumping stage. The pumping beam is tuned

to the $5\,^2S_{1/2}\,F = 2 \longrightarrow 5\,^2P_{3/2}\,F = 2$ transition in ^{87}Rb and is circularly polarized (σ^+ with respect to the quantisation axis). A $400\,\mu$s-long pulse of this light pumps the atoms to the $5\,^2S_{1/2}\,F = 2, m_F = +2$ state used for magnetic trapping. Some 5×10^7 atoms are then re-captured in a wire magnetic trap, at a distance of $\sim 1.8\,$mm from the chip surface, by suddenly switching on 15 A through the centre wire, 15 A through the end wires, a 17 G bias field B_b and a 3 G B_{z-coil}. The frequencies of transverse and longitudinal confinement in this trap are 50 Hz and 15 Hz, respectively, and the trap depth is around 7 G. This trap is then adiabatically compressed and moved to a distance of $200\,\mu$m from the chip surface by ramping the bias field up to 44 G over 400 ms. This enables us to achieve the high elastic collision rates required for evaporative cooling. The transverse and longitudinal trap frequencies in this compressed trap are 500 Hz and 16 Hz, respectively, resulting in magnetically confined clouds with aspect ratios of ~ 30. The temperature of the cloud is a few hundred μK at this stage. Two rf evaporation stages are carried out. First, the rf is ramped exponentially from 30 MHz to 11 MHz, over 3.4 s, with a time constant of 3 s; in the second stage, an exponential sweep from 11 MHz to a variable final rf frequency between 8 MHz and 2 MHz is carried out over several seconds, with a time constant of 5 s. We typically evaporate down to $1 - 70\,\mu$K, with 10^5-10^6 atoms remaining in the trap, and lifetimes of up to 30 s. Curiously, the ionisation gauge controller has to be switched off during the evaporation to eliminate the noise it generates at these radio frequencies.

The cooled atoms are transferred from the wire trap into either one or several videotape magnetic traps in two stages, with durations of 1 s and 300 ms, respectively. In the first transfer stage the centre-wire current is lowered from 15 A to 6 A, the horizontal bias field is decreased from 44 G to 22 G, and the axial field is decreased from 2.8 G to 0 G. In the second transfer stage the currents are lowered to 0 A in the centre wire and 10 A in the end wires, and the bias field is decreased to 2.2 G, leaving the atoms confined in videotape traps $\sim 70\ \mu$m from the chip surface. The temperature of the atoms after evaporation controls the number of videotape traps loaded. A $50\,\mu$K-cloud loads 4 videotape traps at the same temperature with approximately 8×10^5 atoms in the fullest (central) trap, while a $10\,\mu$K-cloud in the wire trap loads a single $10\,\mu$K videotape trap with some 2×10^5 atoms (see figure 6).

Atoms in these videotape traps can then be moved to distances from the chip surface between $20\,\mu$m and $100\,\mu$m by ramping the bias field to a value between 0.5 G and 30 G (typically over 1 s). The longitudinal trap frequency is $\sim 13\,$Hz, and the transverse trap frequencies range between 0.5 kHz and 15 kHz, leading to aspect ratios between 40 and 1000. An additional rf evaporation stage can cool the atoms down to around 500 nK if needed. Lifetimes in excess of 30 s are measured for cold atoms ($\sim 20\,\mu$K) confined in videotape traps $\sim 70\,\mu$m away from the chip surface.

At the end of the experimental sequence, an absorption image of the atoms, either in-trap or after release, is recorded using a resonant imaging beam and a CCD camera. Two imaging set-ups with unit magnification are in place. In set-up A, an imaging beam reflects off the gold-coated surface of the chip at an angle of 14° and propagates
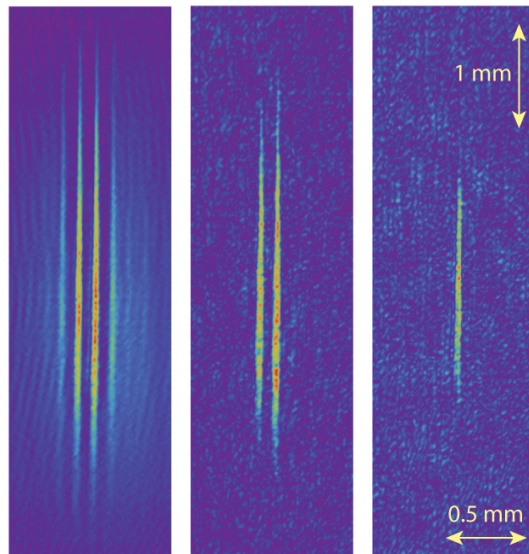
Figure 6. In-trap absorption images of atoms loaded into either one or several videotape traps, acquired using imaging set-up B (see text). From left to right, the final rf frequency of the evaporation ramp in the compressed wire magnetic trap decreases from $8\,\mathrm{MHz}$ to $2.5\,\mathrm{MHz}$, and the temperature of the best-loaded (central) videotape trap decreases from $\sim 50\,\mu\mathrm{K}$ to $\sim 10\,\mu\mathrm{K}$. The length scale is the same for all images.

at $35°$ to the x direction. A double absorption image appears, corresponding to the atomic cloud and its reflection in the chip surface. The atom-surface separation is half the perpendicular distance between these two images. The imaging beam in set-up B propagates in the y-z plane, reflecting off the chip surface at $45°$. The cloud and its reflection are unresolved and form a single image, as shown in figure 6. The oblique viewing is responsible for the different x and z scales in this figure. The spatial resolution is $\sim 7\,\mu\mathrm{m}$ for both arrangements.

4. Fragmentation experiments

A thermal cloud of atoms confined in a corrugated magnetic potential will start breaking into fragments when the thermal energy of the atoms is comparable to the depth of the corrugation, which on a typical atom chip is a few $\mu\mathrm{K}$ for atom-surface separations below $100\,\mu\mathrm{m}$. For a Bose-Einstein condensate (BEC) the relevant energy scale would be the chemical potential instead.

In some cases, this corrugation can turn out to help experiments by, for instance, resulting in tighter confinement [53] or leading to the production of multiple BECs [54]. However, it is worth noting that, in such cases, the landscape of the corrugation is uncontrolled. In other cases, where a smooth trapping potential is required, fragmentation effects are clearly undesirable.

Fragmentation of atom clouds near current-carrying wires, as first reported in references [55–60], is due to a magnetic field component along the wire. This

anomalous component, typically several orders of magnitude smaller than the main transverse component, is due to deviations in the direction of the current flow. Further detailed studies of fragmentation near conducting wires have been reported in references [14–16, 61–67]. In most of these chips, imperfections in the wires, such as edge roughness or bulk defects, were found to be responsible. Substantial improvements in the techniques for micro-fabricating wires on atom chips have led to smoother trapping potentials in the past few years.

Potential roughness has also been observed in atom chips based on permanently magnetized materials, such as videotape [49], magneto-optical films [68] or hard disk [37]. Potential roughness in those cases was attributed to inhomogeneity of the magnetic material.

This section presents a study of axial fragmentation in our videotape magnetic traps. Absorption images of fragmented clouds are analysed to obtain the axial disorder potential at several distances from the videotape surface. The dependence of the rms potential roughness on atom-surface separation is studied and the strength of this roughness is compared to that observed above other types of atom chip. The frequency spectrum of the disorder potential is analysed and the possible origins of fragmentation on our atom chip are discussed. Finally, a method for reducing fragmentation is outlined and discussed in the context of our videotape atom traps.

4.1. Fragmentation above the videotape atom chip

As described in section 2, the periodic, in-plane magnetisation recorded in the videotape along the x direction should generate a magnetic field with components only in the x-y plane (see equation (2.1)). However, we observe fragmentation due to a fluctuating anomalous magnetic field component, ΔB_z, along the axis of the cloud (z). Note that only the z-component of the noise in the trapping field can lead to axial fragmentation. Noise in the other components has a negligible effect since it only causes a slight transverse displacement of the trap centre.

The disorder potential and the anomalous field component, ΔB_z, are obtained by measuring the density profile of an ultra-cold atomic cloud using absorption imaging. For a cloud of atoms in thermal equilibrium at temperature T, the linear density profile, $n(z)$, is proportional to the Maxwell-Boltzmann probability distribution, so that we can write $n(z) = b \exp[-(U_{dis}(z) + U_{trap}(z))/(k_B T)]$, where b is a normalisation constant, k_B is Boltzmann's constant, $U_{dis}(z)$ is the disorder potential and $U_{trap}(z)$ is the intended axial potential. The disorder potential can therefore be expressed as:

$$U_{dis}(z) = -k_B T \ln\left(\frac{n(z)}{b}\right) - U_{trap}(z). \tag{4.1}$$

The axial potential created by the end wires is approximately harmonic in the regions of the trap explored by the atoms, so we can write $U_{trap}(z) \simeq \frac{1}{2}m\omega_z^2(z - z_0)^2$, where m

is the mass of ^{87}Rb, ω_z is the axial oscillation frequency and z_0 is the central position of the cloud.

The ordered component of the potential, $U_{trap}(z)$, is obtained first, by fitting the measured linear density to a gaussian function, $b \exp\left[-(\frac{1}{2}m\omega_z^2(z-z_0)^2)/(k_BT)\right]$, plus a background. The disorder potential is then found by subtracting the smooth harmonic trapping potential from the full potential measured with atoms. On the trap axis, where the transverse magnetic field is zero, the disorder potential is related to the anomalous longitudinal magnetic field by:

$$U_{dis}(z) = \mu \Delta B_z(z). \tag{4.2}$$

We have studied atoms with temperatures of a few μK at distances between $32\,\mu$m and $79\,\mu$m from the chip surface. Absorption images of the trapped atoms, as shown in figures 7 and 8, are recorded at the end of the experimental sequence described in section 3, using imaging set up A.

Figure 7 shows axial density profiles of atom clouds confined $45.5\,\mu$m away from the chip surface. The temperature of the cloud decreases from top to bottom, illustrating how the fragments become more pronounced as the temperature of the atoms becomes comparable with the depth of the disorder potential.
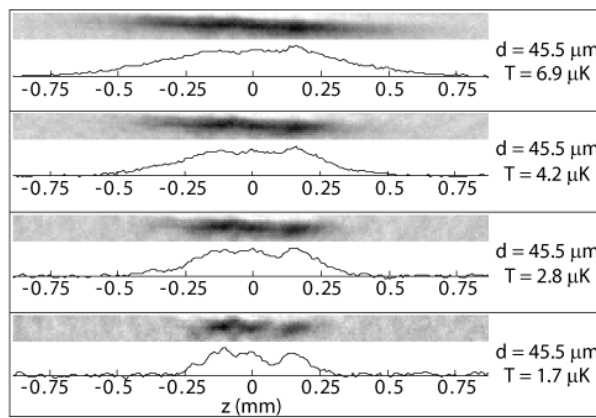

Figure 7. Fragmentation in a videotape atom trap situated a distance d $= 45.5\,\mu$m away from the chip surface. Absorption images and axial linear density profiles for different cloud temperatures, T.

Figure 8 shows atomic clouds with temperatures of the same order of magnitude, around $1-4\,\mu$K, but at different distances from the chip surface. As the atoms move closer to the surface, we see the corrugations becoming stronger.

For each atom-surface separation, d, we record 4-6 absorption images at a range of temperatures between $1.3\,\mu$K and $12.6\,\mu$K. Each image is used to obtain the axial disorder potential making use of equations (4.1) and (4.2). These potentials are averaged to produce the map shown in figure 9. This shows how the axial potential roughness decreases away from the surface, while maintaining the same general shape. At a distance
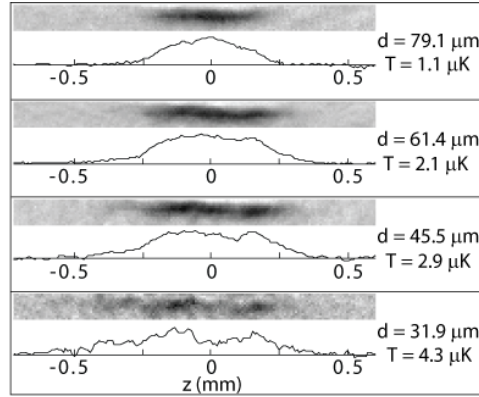
Figure 8. Fragmentation in a videotape atom trap at different distances, d, from the chip surface. The absorption images and axial linear density profiles show how the corrugations in the trapping potential are more pronounced for small atom-surface separations.

of $32\,\mu$m, the peak-to-peak amplitude of the disorder potential is $\sim 3\,\mu$K, decreasing to $\sim 0.2\,\mu$K at $79\,\mu$m.
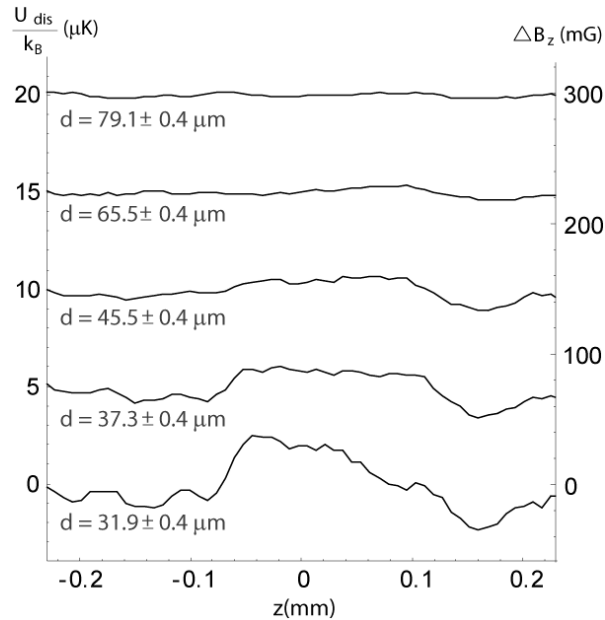

Figure 9. Axial disorder potentials measured with ultra-cold atoms in videotape magnetic traps. Each curve corresponds to a different atom-surface separation, d, that decreases from top to bottom, as indicated by the labels, and is an average of 4-6 experimental realisations. The potentials have been offset vertically from each other by $5\,\mu$K for clarity. The anomalous axial magnetic field, ΔB_z, is calculated using equation (4.2).

Figure 10 shows a log-log plot of the measured rms roughness in μK (and the cor-

responding noise ΔB_z). A linear fit to this graph gives roughness of the form d^{-B}, with $B = 2.7 \pm 0.1$. The magnification of the imaging set-up was 1.0 ± 0.1, introducing a scaling uncertainty of 10% for the horizontal axis in figure 10, but this has no effect on the value of B.
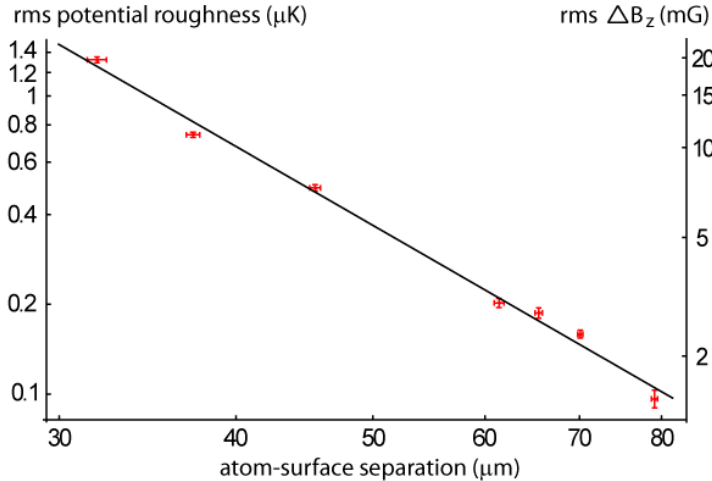

Figure 10. Potential roughness as a function of atom-surface separation d (logarithmic scales). Each data point results from the analysis of 4-6 absorption images coming from different realisations of the experimental sequence. The solid line shows a linear fit of the data that yields a dependence of roughness on atom-surface separation of $d^{-2.7}$.

Several experimental groups that use current-carrying wires to confine cold atoms on a chip have measured the decay of roughness with distance d. Reference [61] found an exponential dependence $\exp(-k_0 d)/\sqrt{k_0 d}$, consistent with an oscillating current flow inside the wire with transverse wavevector k_0. Two papers [64, 65] calculated a dependence of $d^{-2.5}$, valid for distances much larger than the width of the wire, using a model based on white-noise fluctuations of the edges of a flat wire, or of its surface topography. The experimental data presented in references [63, 65] was consistent with this model. The calculations in reference [67] took into consideration the self-affine fractal character of the roughness measured in micro-fabricated wires, as opposed to white-noise fluctuations. Cold atoms confined at distances small compared to the width of the wire [66] showed a decay of potential roughness faster than $d^{-2.5}$. In this case, wire-edge fluctuations were no longer the dominant cause for fragmentation, but instead, inhomogeneous conductivity and top-surface roughness of the wire were more probable explanations.

As for permanent-magnet atom chips, a dependence of $d^{-1.85}$ was measured with cold atoms trapped next to a magneto-optical film [68]. A calculation that included two-dimensional white-noise spatial variations in the magnetisation component perpendicular to the film led to a similar power law of d^{-2}.

Table 1 compares the roughness measured above several atom chips, which we express in temperature units to allow easy comparison with the temperature of the atom cloud. Wires micro-fabricated using lithographic patterning of evaporated gold [65, 66] have proved to be substantially smoother than macroscopic wires or other micro-wires. The roughness of the videotape potential is below that of the other atom chips except for reference [66].

Table 1. Comparison of measured rms potential roughness for different experimental groups working on atom chips.

rms roughness	$d(\mu$m$)$	Atom chip	ref / group
$\sim 2\ \mu$K	40	Macroscopic wire, 0.5 mm diameter.	[61]/Hinds
$\sim 2\ \mu$K	33	Gold electroplated micro-wire.	[63]/Aspect
a few μK	45	Silver foil wires, micro-cut.	[62]/R.-Dunlop
a few μK	4	Micro-wires: lithography + gold evaporation.	[66]/Schmiedmayer
$\sim 7\ \mu$K	60	TbGdFeCo multilayer magnetic film.	[68]/Hannaford
$\sim 0.5\ \mu$K	45	Videotape	this paper/Hinds

The Fourier spectra of our disorder potentials are presented in figure 11 for several atom-surface separations. The power of all frequency components increases at smaller atom-surface separation. At a given value of d, the most important contributions are from wavelengths $\gtrsim d$. We do not detect potential variations on a length scale much less than the $7\,\mu$m imaging resolution. Similar spectra have been observed in several other atom-chip experiments [63, 65, 66, 68].
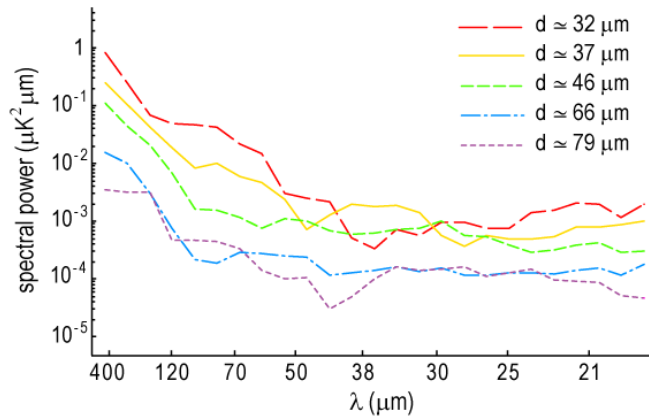

Figure 11. Fourier power spectra of the disorder potentials measured in the videotape traps for different atom-surface separations, d.

4.2. Origin of fragmentation in the videotape atom chip

In considering the origin of roughness, we distinguish two effects. (i) The tape could be wrinkled or the magnetic layer could have varying thickness. (ii) The magnetic material could be inhomogeneous due to density variations or defects.
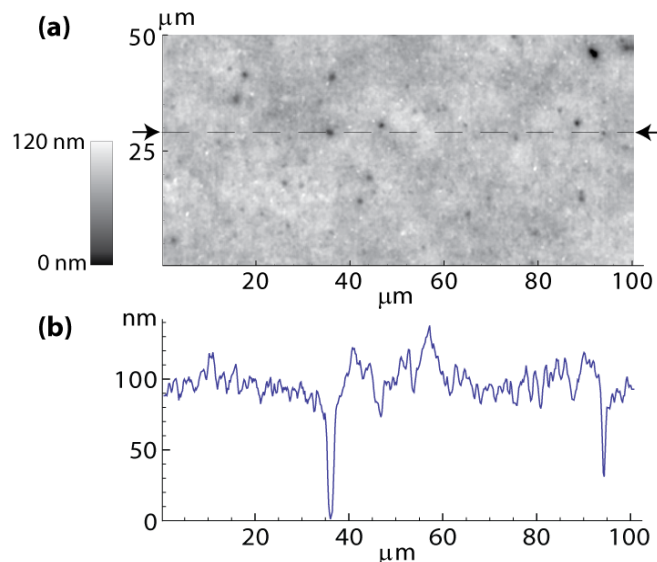

Figure 12. Atomic force microscope scan showing the topography of a piece of videotape. **(a)** Survey of a $100\,\mu$m $\times$ $50\,\mu$m region. **(b)** Height versus position along the line indicated in (a).

The surface topography of the magnetic layer of a piece of videotape was inspected using an atomic force microscope (AFM), as shown in figure 12. Height variations of up to 20 nm were found with wavelengths of the order of tens of microns. These could result from the inability of the videotape to lie completely flat or from variations in its thickness. The AFM scans also revealed some deeper holes in the surface of the magnetized layer that were typically around 100 nm deep and a few μm wide [49]. The $3.5\,\mu$m-thick magnetic layer of the videotape consists of iron-composite needles 100 nm in length and 10 nm in radius, embedded in glue and aligned parallel to each other along the x direction. A hole such as the deep ones observed on the AFM scans would constitute a magnetisation defect with hundreds of magnetized needles missing. The magnetic field created by the videotape directly below one of these defects would have a non-zero component along the z direction [69]. It seems most probable that the combined effects of height and thickness variations and defects in the videotape are responsible for the measured fluctuations in the z-component of the total magnetic field. The videotape used in our experiment has the smoothest surface topography of several types ¶ inspected through atomic force microscopy.

¶ We have inspected the following digital videotapes: Quantegy DBC-D12A, Quantegy D2V-126LC and Fuji D2001-D-2-S-12. Analog videotape is no longer commercially available.

4.3. Suppressing fragmentation in the videotape atom chip

The fragmentation described above constitutes an important obstacle to studies of one-dimensional (1D) quantum gases on this chip. Since the large transverse trap frequencies required to enter the 1D regime can only be achieved at small atom-surface separations, an effective mechanism for suppressing fragmentation would prove an extremely useful tool for the progress of such experiments.

As reported in references [70,71], fragmentation can be reduced in a current-carrying wire atom chip by rapid reversal of the currents through the trapping and bias wires. This reverses ΔB_z, so that the time-averaged potential has a reduced roughness. In our experiment, we cannot reverse ΔB_z, but we can instead overwhelm it with a rotating transverse field, as we describe below.

We propose reducing B_z to zero, which gives a two-dimensional, transverse quadrupole field. A rotating magnetic field B_{rot}, added in the transverse plane, causes the magnetic field minimum to describe a circle. If the rotation frequency is high enough compared to the trapping frequencies [+] and low enough compared to the Larmor frequency, the atoms are unable to follow the movement of the field minimum and feel a time-averaged potential. The result is a TOP (time-averaged orbiting potential) trap [72], in which the time average over one field rotation yields a parabolic transverse potential close to the trap centre, with the field at the bottom of the trap being equal to B_{rot}:

$$|\vec{B}(r)| \approx B_{rot} + \frac{\alpha^2}{4B_{rot}} r^2 \,, \tag{4.3}$$

where $\alpha = kB_b$ is the gradient of the static transverse quadrupole field. From equation (4.3) we deduce that the frequency of transverse oscillations in the TOP trap is $f_{r-TOP} = \sqrt{B_z/(2B_{rot})}f_r$, where f_r is the frequency in a static trap with axial field B_z, given by equation (2.4).

The transverse field strength at the bottom of the time-averaged potential is B_{rot}, and the z-component from the end wires, assumed to be harmonic, is βz^2, so that:

$$|\vec{B}(r = 0, z)| = \sqrt{B_{rot}^2 + (\beta z^2)^2} \approx B_{rot} + \frac{\beta^2}{2B_{rot}} z^4 \,. \tag{4.4}$$

This shows that the harmonic axial confinement is now flattened to the more box-like form z^4, offering interesting possibilities for studies of one-dimensional quantum gases [73].

Adding the noise field, ΔB_z, equation (4.4) becomes:

$$|\vec{B}(r = 0, z)| = \sqrt{B_{rot}^2 + (\Delta B_z + \beta z^2)^2} \,. \tag{4.5}$$

[+] strictly speaking, we should also compare to the actual oscillation frequencies of the atoms inside the fragments, since these may be considerably higher than the nominal trapping frequencies

If we choose B_{rot} to be large compared to $(\Delta B_z + \beta z^2)$,

$$|\vec{B}(r = 0, z)| \approx B_{rot} + \frac{\beta^2}{2B_{rot}}z^4 + \left(\frac{\Delta B_z}{2B_{rot}} + \frac{\beta z^2}{B_{rot}}\right)\Delta B_z, \qquad (4.6)$$

where the first two terms duplicate equation (4.5) and the last term is the roughness suppressed by the factor $\left(\frac{\Delta B_z}{2B_{rot}} + \frac{\beta z^2}{B_{rot}}\right)$. Near the bottom of the axial potential this factor is approximately $\Delta B_z/(2B_{rot})$.
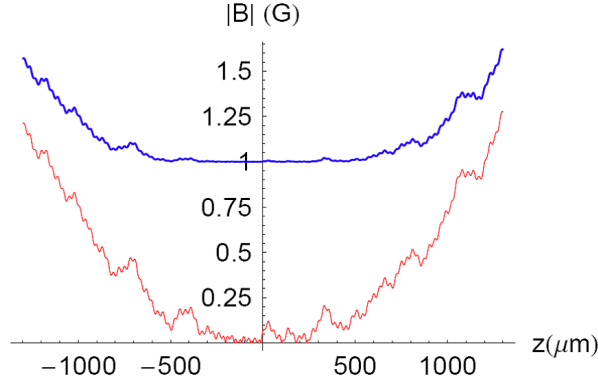

Figure 13. Predicted reduction of the axial potential roughness by cancelling the net axial offset field and superimposing a rotating transverse field of $1\,\text{G}$. The thin red line shows the static magnetic field strength with disorder, including the end-wire field, before the rotating field is added. The thicker blue line shows the time-averaged field strength after adding the rotating field.

Figure 13 shows a calculated example of this smoothing method in a trap $\sim 22\,\mu\text{m}$ from the chip surface ($I_{end} = 15\,\text{A}$, $B_b = 30\,\text{G}$, $B_{z-coil} = 4.73\,\text{G}$ and $B_z = 0\,\text{G}$). At this height the rms field corrugation would be of order $50\,\text{mG}$ ($3.3\,\mu\text{K}$). The total magnetic field modulus is plotted as a function of the position, z, along the axis of the trap. The thin red curve shows the field strength before the rotating field is included. A $1\,\mu\text{K}$ atom cloud would appear strongly fragmented in such a trap. The thicker blue curve shows the resulting time-averaged field strength after a rotating field, $B_{rot} = 1\,\text{G}$, is applied. The field fluctuations are strongly reduced in the central region of the trap, where $(\Delta B_z + \beta z^2) < B_{rot}$, the maximum reduction factor being $1/40$ at $z = 0$. The graph also shows how the field at the bottom of the trap is raised by an offset equal to B_{rot}, as given by equation (4.6). For the chosen values of B_b and B_{rot}, the transverse frequency in the time-averaged potential would be $f_{r-TOP} \sim 16\,\text{kHz}$, of the same order of magnitude as the transverse frequency in the static trap ($23\,\text{kHz}$) with $B_z = 1\,\text{G}$. Considering this frequency and the Larmor frequency of a few MHz, a transverse rotating field with a frequency of order $50\,\text{kHz}$ would be a good choice. Note that we require $B_{rot} \gg 4k_B T/\mu_B$, where T is the temperature of the atoms in the trap, in order to prevent the atoms reaching the circle of zero field [72]. For a $1\,\mu\text{K}$ cloud, this implies $B_{rot} \gg 0.06\,\text{G}$, which is amply satisfied in the example above.

This possibility of maintaining large transverse trap frequencies together with a flatter axial potential and a strong suppression of the potential roughness makes our videotape traps interesting for possible future studies of 1D quantum gases.

5. Transport experiments

The possibility of moving atoms from one region to another promises to enhance the functionality of atom chip devices. For this reason transport has been studied by several groups.

Transport of cold atoms along small magnetic guides on a chip has been reported in references [2, 58, 74]. The group of T. W. Hänsch and J. Reichel [75–78] realised a magnetic conveyor belt for moving atoms trapped in 3D across a chip over distances of many cm. A similar chip set up which demonstrated adiabatic transport of a $6\,\mu$K thermal cloud over several mm is reported in reference [79]. The group of R. J. C. Spreeuw [80] displaced atoms up to a round-trip distance of $360\,\mu$m, in a two-dimensional array of hundreds of tight traps generated by a permanently magnetised FePt film.

We have now brought similar capability to our chip by implementing the effective transport of cold atoms over long distances up to ~ 1 cm while they remain confined in all three dimensions. This is achieved by rotating the direction of the applied bias field in order to translate the traps along x, as proposed in [43–45, 81]. We have used this capability to survey the chip surface in our study of disorder above different regions of the videotape, as discussed in section 5.2.

5.1. Transport mechanism

At a fixed distance from the chip surface, the magnetic field created by the magnetized videotape has constant modulus and its direction rotates as one moves along x, as given by equation (2.1). Since the traps are centred on the lines where the bias field cancels the videotape field, a rotation of the bias field translates the traps along the x-direction, as illustrated by figure 14. One full rotation translates the traps by one spatial period $\lambda \sim 110\,\mu$m, giving a translation velocity $v_x = \lambda\Omega/(2\pi)$, where $\Omega/(2\pi)$ is the rotation frequency of the bias field.

It is important to consider the contribution of all the magnetic fields that confine the atoms during a transport cycle. In particular, the y-component of the field created by the end wires (see figure 4) changes sign as we move along the z axis and cross $z = 0$, where its value is zero. This gives rise to a bending of the trap axis and to a variation of the transverse trap frequencies along the trap axis, causing a transverse compression at one end of the trap and de-compression at the opposite end. Both effects depend on the direction of the bias field. As a consequence, two dynamic effects take place during transport: there is an oscillating bend of the trap axis, and a periodic transverse compression and de-compression of the trap ends. In addition there is a small periodic
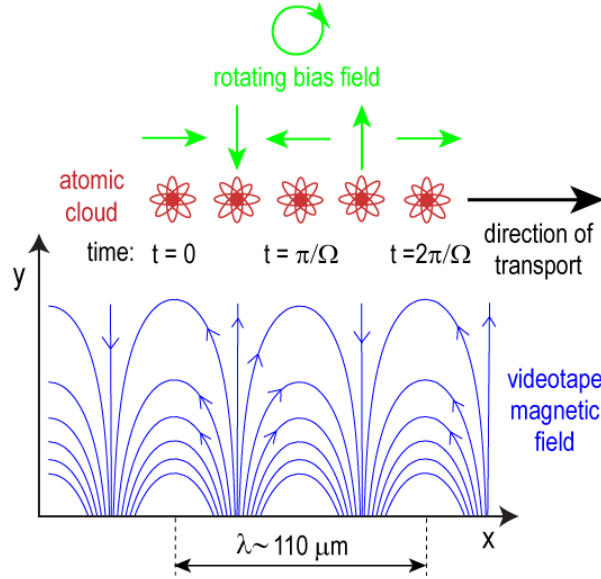
Figure 14. Transport mechanism used to displace the trapping potential along x. The videotape magnetic field lines are shown in blue and the rotating bias field in green. As the orientation of the bias field changes in time during one rotation, the traps translate along x by a distance equal to λ. $\Omega/(2\pi)$ is the bias-field rotation frequency.

movement of the trap centre. These effects are explained in more detail below.

The line of minimum potential energy of the trap, denoted as ζ axis, is bent and evolves during transport as shown in figure 15. The line ζ is calculated numerically by finding the minimum of the potential energy in the x-y plane (including gravity) for a given z value, then moving along z between $z = \pm 2\,\mathrm{mm}$. We exaggerate the effect by plotting mm along z and μm along the other axes.

When the bias field is along the x direction (red and light-blue lines in figure 15, at $x = 0, \pm 55\,\mu\mathrm{m}, \pm 110\,\mu\mathrm{m}$), the trap is mostly curved horizontally on the x-z plane because the y-field from the end wires is up at one end and down at the other. This rotates the net bias field oppositely at the two ends, displacing the trap towards $+x$ at one end and $-x$ at the other. At the ends of the trap, where $|z| \sim 2\,\mathrm{mm}$, the trap height also decreases by a few micrometres, due to the increase of the total modulus of the bias field caused by the added y-component of the end-wire field. When the bias field is along the y direction (light-green and purple lines in figure 15, at $x = \pm 27.5\,\mu\mathrm{m}, \pm 82.5\,\mu\mathrm{m}$), the bending of the trap is vertical, on the y-z plane, since the y-component of the end-wire field simply adds to the total bias field, increasing its magnitude on one side of $z = 0$ and decreasing it on the other. For the two cases described above, the tilt angles near the trap centre are $\sim 1°$.

Figure 16 shows a 3D plot of a contour of constant potential energy (equivalent to $230\,\mu\mathrm{K}$), during a transport sequence corresponding to the same two full rotations of the bias field. As the elongated trap progresses from $x = -110\,\mu\mathrm{m}$ to $x = 110\,\mu\mathrm{m}$, we
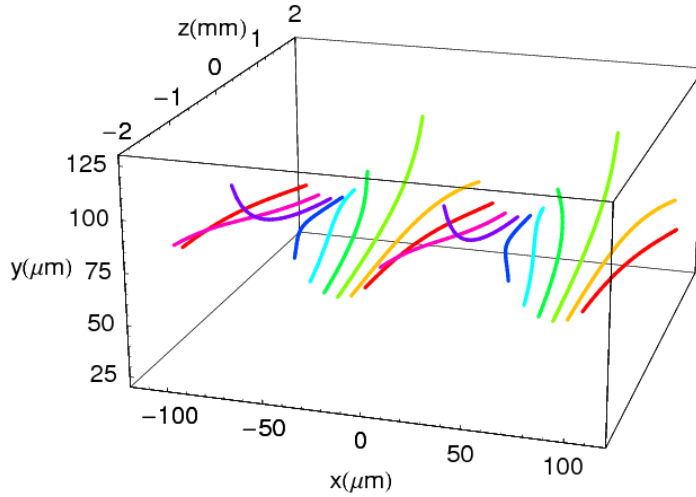
Figure 15. Line of minimum potential energy (ζ) as seen in 3D during two cycles of bias-field rotation for the transport of atoms in videotape traps with $\lambda = 110\,\mu\text{m}$, $B_b = 2.2\,\text{G}$, $B_{z-coil} = 0$ and $I_{end} = 10\,\text{A}$, corresponding to our experimental parameters. Gravity is included in the calculation.
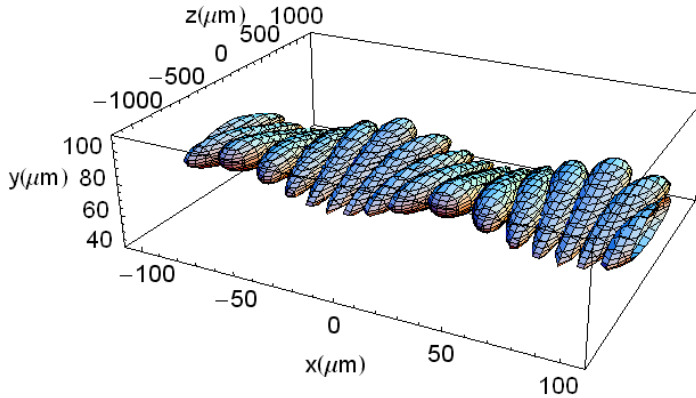

Figure 16. Contour of constant potential energy ($230\,\mu\text{K}$) over two full transport cycles. Parameters of the calculation are those used in experiments: $\lambda = 110\,\mu\text{m}$, $B_b = 2.2\,\text{G}$, $B_{z-coil} = 0$ and $I_{end} = 10\,\text{A}$, and gravity is included. Each contour corresponds to a different time during transport.

observe a movement of the trap ends resembling the pedals of a bicycle, with each end describing an ellipse in the x-y plane. The angular acceleration of the atoms at the ends of the trap due to this movement can result in transport-induced heating.

At the positions where ζ bends vertically, there is significant variation along the trap of the transverse confinement, which is tighter at the ends closer to the videotape (due to the increased effective bias field, see equation (2.4)), and more relaxed at the opposite ends. This can be seen in figure 16, and is further illustrated by figure 17, which shows the contours of constant potential energy in the videotape traps on the

$x - \zeta$ and $\zeta - y$ surfaces, as we move along ζ. The periodic transverse compression and de-compression of the trap ends induces an axial oscillation of the cloud (as detailed in the next section), as well as transverse excitations, heating the atoms during transport. These effects are more pronounced when the clouds being transported are hot since the change in shape of the energy equipotentials during one rotation of the bias field is more dramatic the further the atoms are from the trap axis.
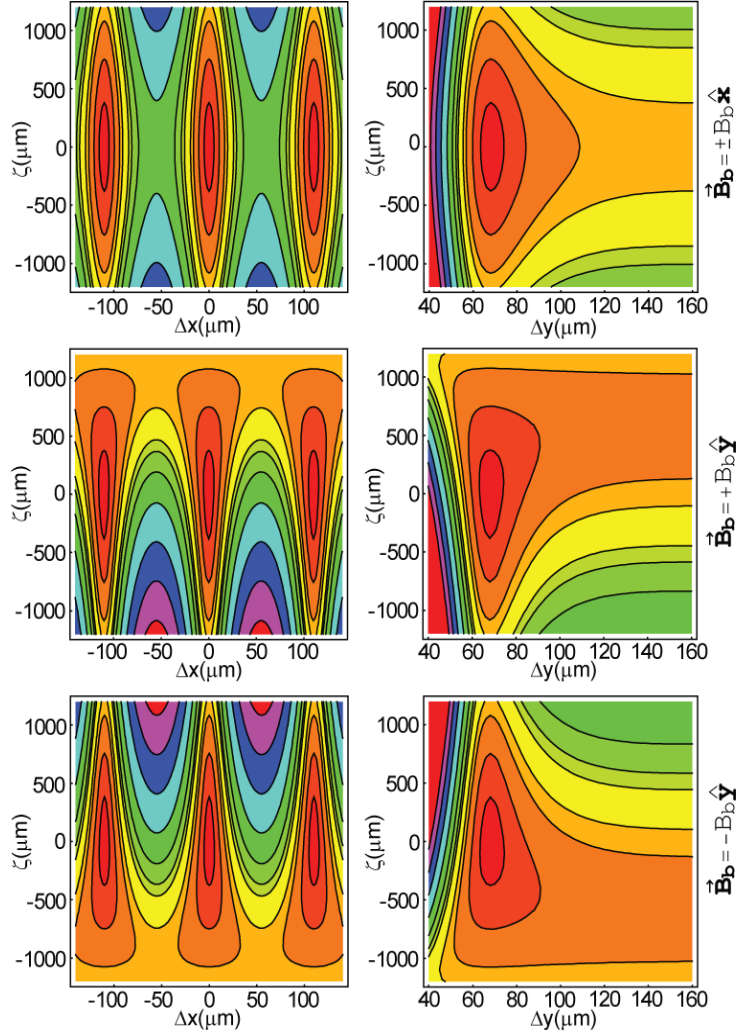

Figure 17. Contours of constant potential energy (between $220\,\mu$K and $940\,\mu$K). Cross-sections through the $x - \zeta$ and $\zeta - y$ surfaces are shown on the left- and right-hand sides respectively. Δx and Δy are the distances to the effective trap axis, ζ, along the x and y directions, respectively. From top to bottom the bias fields are: $\vec{B}_b = \pm B_b \hat{\mathbf{x}}$, $\vec{B}_b = +B_b \hat{\mathbf{y}}$ and $\vec{B}_b = -B_b \hat{\mathbf{y}}$. The parameters used in these plots are: $\lambda = 110\,\mu$m, $B_b = 2.2\,$G, $B_{z-coil} = 0$ and $I_{end} = 10\,$A. Gravity is included in the calculation.

The trap centres hardly deviate from the straight-line path along x that we would expect for smooth transport. The y-coordinate of the trap centre oscillates with a

very small amplitude of $\sim 14\,\text{nm}$ at twice the bias-field-rotation frequency, while the z-coordinate of the trap centre oscillates with an amplitude of $\sim 2.2\,\mu\text{m}$, at the bias-rotation frequency. The end-wire field is again responsible for these effects. The minimum potential energy calculated at the bottom of the trap stays constant during transport to within $1\,\text{nK}$. These periodic variations of the trap centre during transport are very small and do not excite the atomic cloud appreciably.

5.2. Experimental data

Figure 18 shows absorption images of atoms confined in an array of 5-6 elongated videotape traps at temperatures around $500\,\mu\text{K}$, transported up to $1\,\text{mm}$ along x as the bias field goes through 0 to 9 rotation cycles at a frequency of $50\,\text{Hz}$. The bias field is $19\,\text{G}$ and the distance from the traps to the chip surface during transport is $30\,\mu\text{m}$.
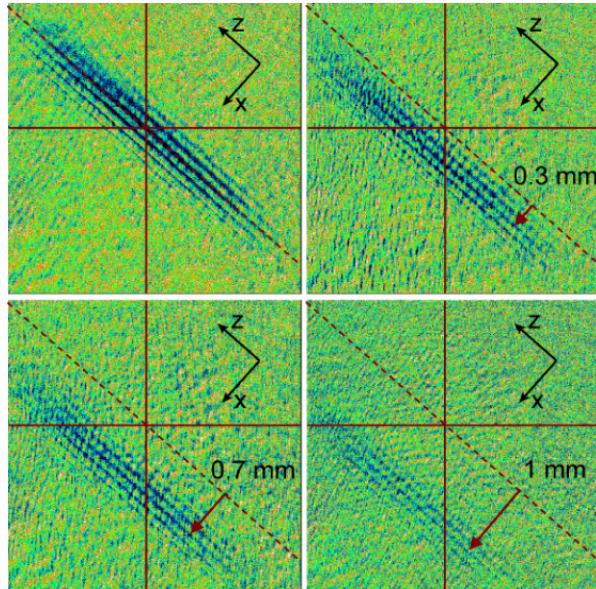

Figure 18. Absorption images of an array of 5-6 videotape magnetic traps transported parallel to the chip surface, along the x direction. From the top left, the transported distances are: 0, $0.3\,\text{mm}$, $0.7\,\text{mm}$ and $1\,\text{mm}$, corresponding to 0, 3, 6 and 9 cycles of bias field rotation at a frequency of $50\,\text{Hz}$. The solid and dashed lines are fixed at the same position on all images.

The obvious atom loss that we observe in figure 18 is due in part to the fact that these traps are loaded without an rf-evaporation stage in the wire trap (see section 3). Therefore, the ratio of videotape trap depth to atomic thermal energy is only 2, leading to an important loss rate by evaporation. Additionally, the transport-induced excitations heat the atoms, enhancing the loss. After one transport cycle we measure an induced axial dipole oscillation of the centre of mass of the cloud with an amplitude of $300\,\mu\text{m}$.

When we use the optimized loading sequence described in section 3 and cool the

atoms before conveying them, we achieve much longer transport distances. After an rf evaporation stage in the wire trap, the atoms are loaded into two videotape traps with transverse frequencies of $1.5\,\mathrm{kHz}$ and an axial frequency of $13\,\mathrm{Hz}$, at a distance of $68\,\mu\mathrm{m}$ from the chip surface. An additional rf ramp cools the atoms down to temperatures between $6\,\mu\mathrm{K}$ and $66\,\mu\mathrm{K}$. These atoms are then transported across the surface of the chip over a distance of $\sim 1\,\mathrm{cm}$ using a bias field of $2.2\,\mathrm{G}$ rotating at a frequency of $50\,\mathrm{Hz}$, to produce a transport velocity of $6\,\mathrm{mm/s}$. The magnitude of the bias field remains constant to within 2% during the rotation.

Figure 19 shows a sequence of absorption images of a few times 10^5 atoms initially at $16\,\mu\mathrm{K}$, confined in two videotape traps and transported over $4.4\,\mathrm{mm}$ to the right, and over $2\,\mathrm{mm}$ to the left of their initial position on the image plane, corresponding to 40 and 18 full rotations of the bias-field direction, respectively. The camera is not moved during the process of data taking and the same region of interest is shown on all images. The clouds are transported until they leave the field of view on both sides of the image, with no significant atom loss.

Colder atom clouds with temperatures around $6\,\mu\mathrm{K}$ have been transported over even larger distances, up to $7\,\mathrm{mm}$ (65 bias-field-rotation cycles) towards the right, and $4\,\mathrm{mm}$ (36 cycles) towards the left-hand side, covering half the $22\,\mathrm{mm}$ length of videotape on the chip (data not shown).

We find that the inhomogeneities of the axial trapping potential change noticeably, both in shape and magnitude, as the atoms are transported to different locations away from the chip centre. In one region, after a transport distance of $\sim 1.5\,\mathrm{mm}$, each atom cloud divides axially into two, separated by $\sim 1.75\,\mathrm{mm}$, which then merge again as shown by the sequence of absorption images in figure 20. Each image corresponds to a different experimental realisation in which two neighbouring clouds of atoms are conveyed over an odd number of transport cycles, from 7 to 21. The whole montage shows the clouds as they are physically positioned below the videotape. The clouds have a temperature of order $30\,\mu\mathrm{K}$. Where they split, the potential roughness has an amplitude of up to $50\,\mu\mathrm{K}$ - much more than the few $\mu\mathrm{K}$ measured in section 4.

It is possible to cool the atoms by rf evaporation after having transported them. Figure 21 shows a sequence of four absorption images recorded after the atoms are first conveyed over 19 transport cycles, i.e., over a distance of $2\,\mathrm{mm}$, and then cooled in the videotape traps for up to $2\,\mathrm{s}$. From left to right, the temperature of the atoms is reduced by a factor of 10. Evaporating after transport makes the potential roughness in this region more obvious, as already seen in section 4.

We notice that the transport process induces a clear axial excitation of the clouds. Figure 22 shows the amplitude of axial oscillation of the centre of mass of the cloud, measured after one transport cycle, as a function of initial temperature. This amplitude decreases as the initial temperature of the cloud is lowered by rf evaporation before transport. This behaviour is consistent with the motion being driven by the compression and relaxation of the trap ends during transport. Indeed, a rough estimate of this
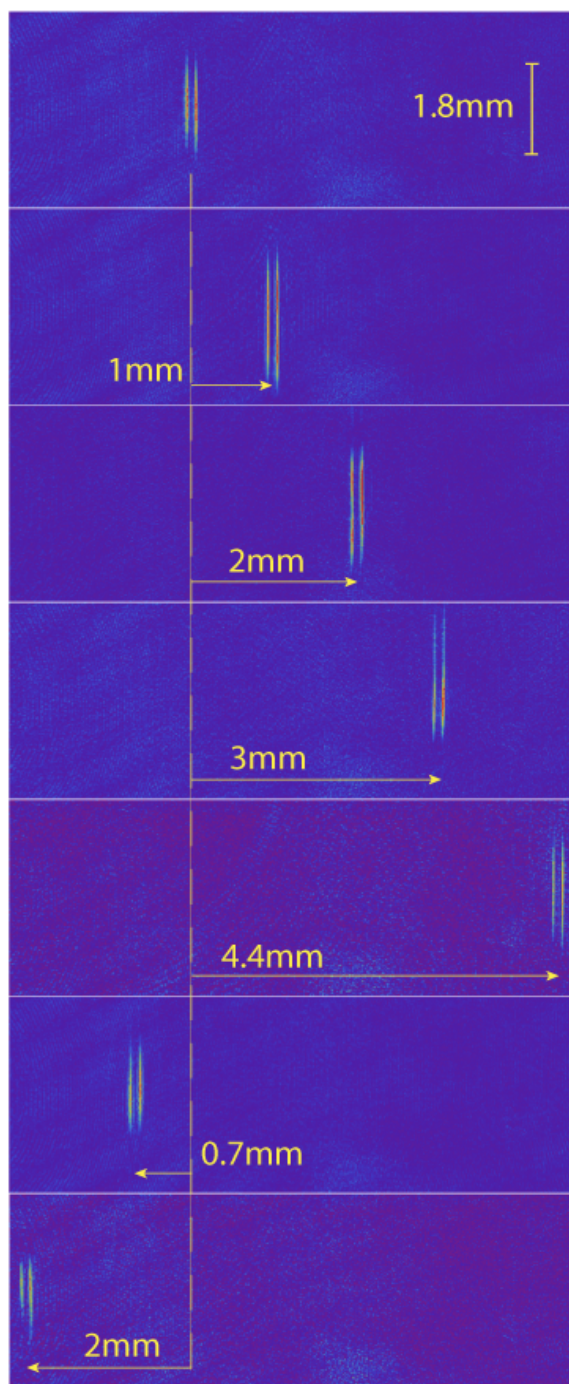
Figure 19. Sequences of absorption images of cold atoms $(16\,\mu\mathrm{K})$ confined in two videotape traps and transported to either side of their initial loading position over the distances indicated. The frequency of bias field rotation is $50\,\mathrm{Hz}$, and the trap height is $68\,\mu\mathrm{m}$.

type of heating captures well the observed trend of decreasing amplitude with lower temperature. The energy in this axial oscillation is responsible for heating the cloud. For example a sloshing amplitude of $400\,\mu\mathrm{m}$ dissipates to produce a temperature rise of
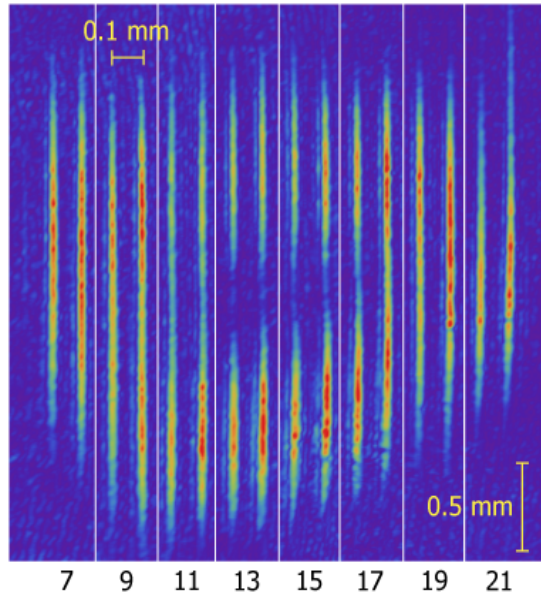
Figure 20. Absorption images of atoms transported from left to right, following the same experimental sequence as for the images in figure 19. Two videotape traps are initially loaded and simultaneously transported. From left to right, the clouds are conveyed over 7 to 21 transport cycles, as indicated by the numbers below the images, corresponding to distances between 0.8 mm and 2.3 mm. The atom-surface separation is 68 μm.
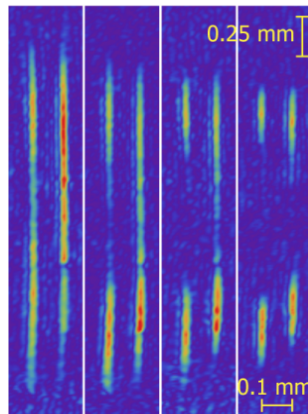

Figure 21. Sequence of four absorption images of two clouds of atoms confined in videotape traps, after they are transported over 2 mm (19 cycles) and then evaporated to different final temperatures. From left to right, the time duration of the rf sweep increases from 0 to 2 s, and the temperature is reduced by a factor of 10, revealing the inhomogeneities of the trapping potential in this region of the videotape.

order 2 μK per cycle, which agrees well with the heating rates we observe for clouds that are initially hot. By contrast, clouds that are initially cold have low sloshing amplitudes and are not heated substantially by this mechanism. However we do observe heating of these clouds, indicating that some other mechanism is operating as well. We have
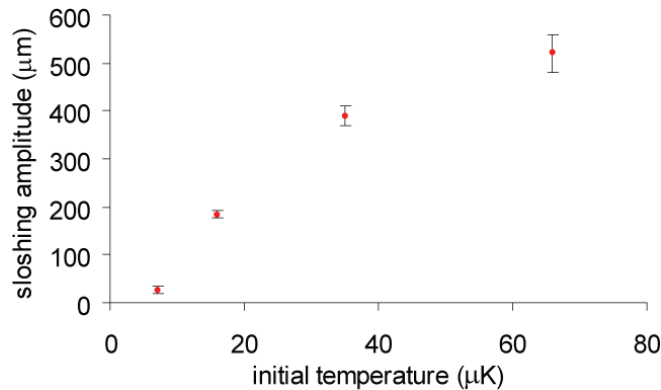
Figure 22. Measured amplitude of the transport-induced, axial dipole oscillations of the clouds, after one transport cycle, as a function of the initial temperature in the videotape traps before transport.

considered heating due to the initial acceleration, to the circular movement of the trap ends and to driving the cloud over the roughness of the potential. Since all of these mechanisms produce negligible heating, we presume that there is a technical cause for the measured heating that remains to be discovered. At present our heating rate is small enough to permit transport of atom clouds with temperatures of a few μK over distances of a few hundred micrometres and we see no fundamental obstacle in the future to transporting Bose-Einstein condensates in this way over long distances.

6. Conclusions

The results presented in this paper explain how permanently magnetized videotape mounted on an atom chip can be used for trapping, cooling and transporting ultra-cold neutral atoms.

We have demonstrated experimentally the transport of cold atoms in arrays of traps over distances as large as 1 cm. Our transport mechanism enables us to survey the chip surface and choose a region where potential roughness is small.

We have shown that the videotape potential is smooth enough to allow a wide range of experiments with cold atoms, and that the potential roughness is quite low compared with other atom-chip experiments (with the exception of reference [66]). Furthermore, we have proposed a method to reduce fragmentation in our traps, which could make our chip suitable for studies of one-dimensional quantum gases.

Acknowledgments

References

[1] Reichel J, Hänsel W and Hänsch T W 1999 *Phys. Rev. Lett.* **83** 3398
[2] Folman R, Krüger P, Cassettari D, Hessmo B, Maier T and Schmiedmayer J 2000 *Phys. Rev. Lett.* **84** 4749
[3] Schumm T, Hofferberth S, Andersson L M, Wildermuth S, Groth S, Bar-Joseph I, Schmiedmayer J and Krüger P 2005 *Nature Physics* **1** 57
[4] Günther A, Kraft S, Zimmermann C and Fortágh J 2007 *Phys. Rev. Lett.* **98** 140403
[5] Jo G B, Choi J H, Christensen C A, Lee Y R, Pasquini T A, Ketterle W and Pritchard D E 2007 *Phys. Rev. Lett.* **99** 240406
[6] Esteve J, Trebbia J B, Schumm T, Aspect A, Westbrook C I and Bouchoule I 2006 *Phys. Rev. Lett.* **96** 130403
[7] Trebbia J B, Esteve J, Westbrook C I and Bouchoule I 2006 *Phys. Rev. Lett.* **97** 250403
[8] Hofferberth S, Lesanovsky I, Fischer B, Schumm T and Schmiedmayer J 2007 *Nature* **449** 324
[9] van Amerongen A H, van Es J J P, Wicke P, Kheruntsyan K V and van Druten N J 2008 *Phys. Rev. Lett.* **100** 090402
[10] Hofferberth S, Lesanovsky I, Schumm T, Imambekov A, Gritsev V, Demler E and Schmiedmayer J 2008 *Nature Physics* **4** 489
[11] Jones M P A, Vale C J, Sahagun D, Hall B V and Hinds E A 2003 *Phys. Rev. Lett.* **91** 080401
[12] Lin Y, Teper I, Chin C and Vuletić V 2004 *Phys. Rev. Lett.* **92** 050404
[13] Scheel S, Rekdal P K, Knight P L and Hinds E A 2005 *Phys. Rev. A* **72** 042901
[14] Wildermuth S, Hofferberth S, Lesanovsky I, Haller E, Andersson L M, Groth S, Bar-Joseph I, Krüger P and Schmiedmayer J 2005 *Nature* **435** 440
[15] Wildermuth S, Hofferberth S, Lesanovsky I, Groth S, Krüger P, Schmiedmayer J and Bar-Joseph I 2006 *Appl. Phys. Lett.* **88** 264103
[16] Aigner S, Pietra L D, Japha Y, Entin-Wohlman O, David T, Salem R, Folman R and Schmiedmayer J 2008 *Science* **319** 226
[17] Scheel S, Fermani R and Hinds E A 2007 *Phys. Rev. A* **75** 064901
[18] Knappe S, Schwindt P D D, Shah V, Hollberg L, Kitching J, Liew L and Moreland J 2005 *Optics Express* **13** 1249
[19] Lacroûte C, Reinhard F, Ramirez-Martinez F, Deutsch C, Schneider T, Reichel J and Rosenbusch P 2010 *IEEE Transactions on Ultrasonics, Ferroelectrics and Frequency Control* **57** 106
[20] Treutlein P, Steinmetz T, Colombe Y, Hommelhoff P, Reichel J, Greiner M, Mandel O, Widera A, Rom T, Bloch I and Hänsch T W 2006 *Fortschr. Phys.* **54** 702
[21] Trupke M, Metz J, Beige A and Hinds E A 2007 *Journal of Modern Optics* **54** 1639
[22] Krüger P, Haase A, Andersson L M and Schmiedmayer J 2002 *Journal of Modern Optics* **49** 1375
[23] Takamizawa A, Steinmetz T, Delhuille R, Hänsch T W and Reichel J 2006 *Optics Express* **14** 10976
[24] Colombe Y, Steinmetz T, Dubois G, Linke F, Hunger D and Reichel J 2007 *Nature* **450** 272
[25] Teper I, Lin Y J and Vuletić V 2006 *Phys. Rev. Lett.* **97** 023002
[26] Purdy T P and Stamper-Kurn D M 2008 *Appl. Phys. B* **90** 401
[27] Heine D, Wilzbach M, Raub T, Hessmo B and Schmiedmayer J 2009 *Phys. Rev. A* **79** 021804(R)
[28] Trupke M, Goldwin J, Darquié B, Dutier G, Eriksson S, Ashmore J and Hinds E A 2007 *Phys. Rev. Lett.* **99** 063601
[29] Pollock S, Cotter J P, Laliotis A and Hinds E A 2009 *Opt. Express* **17** 14109
[30] Kohnen M, Succo M, Petrov P G, Nyman R A, Trupke M and Hinds E A 2010 *arXiv:0912.4460*
[31] Fortágh J and Zimmermann C 2007 *Rev. Mod. Phys.* **79** 235

[32] Hall B V, Whitlock S, Scharnberg F, Hannaford P and Sidorov A 2006 *J. Phys. B: At. Mol. Opt. Phys.* **39** 27

[33] Singh M, Volk M, Akulshin A, Sidorov A, McLean R and Hannaford P 2008 *J. Phys. B: At. Mol. Opt. Phys.* **41** 065301

[34] Barb I, Gerritsma R, Xing Y T, Goedkoop J B and Spreeuw R J C 2005 *Eur. Phys. J. D* **35** 75

[35] Gerritsma R, Whitlock S, Fernholz T, Schlatter H, Luigjes J A, Thiele J U, Goedkoop J B and Spreeuw R J C 2007 *Phys. Rev. A* **76** 033408

[36] Fernholz T, Gerritsma R, Whitlock S, Barb I and Spreeuw R J C 2008 *Phys. Rev. A* **77** 033409

[37] Boyd M, Streed E W, Medley P, Campbell G K, Mun J, Ketterle W and Pritchard D E 2007 *Phys. Rev. A* **76** 043624

[38] Jaakkola A, Shevchenko A, Lindfors K, Hautakorpi M, Il'yashenkoa E, Johansen T H and Kaivola M 2005 *Eur. Phys. J. D* **35** 81

[39] Shevchenko A, Heiliö M, Lindvall T, Jaakkola A, Tittonen I, Kaivola M and Pfau T 2006 *Phys. Rev. A* **73** 051401(R)

[40] Hughes I G, Barton P A, Roach T M, Boshier M G and Hinds E A 1997 *J. Phys. B: At. Mol. Opt. Phys.* **30** 647

[41] Hughes I G, Barton P A, Roach T M and Hinds E A 1997 *J. Phys. B: At. Mol. Opt. Phys.* **30** 2119

[42] Saba C V, Barton P A, Boshier M G, Hughes I G, Rosenbusch P, Sauer B E and Hinds E A 1999 *Phys. Rev. Lett.* **82** 468

[43] Rosenbusch P, Hall B V, Hughes I G, Saba C V and Hinds E A 2000 *Appl. Phys. B* **70** 709

[44] Hinds E A and Hughes I G 1999 *J. Phys. D: Appl. Phys.* **32** R119

[45] Hinds E A 1999 *Phil. Trans. R. Soc. Lond. A* **357** 1409

[46] Ghanbari S, Kieu T D and Hannaford P 2007 *J. Phys. B: At. Mol. Opt. Phys.* **40** 1283

[47] Eriksson S, Ramirez-Martinez F, Curtis E A, Sauer B E, Nutter P W, Hill E W and Hinds E A 2004 *Appl. Phys. B* **79** 811

[48] Sinclair C D J, Curtis E A, Llorente García I, Retter J A, Hall B V, Eriksson S, Sauer B E and Hinds E A 2005 *Phys. Rev. A* **72** 031603(R)

[49] Sinclair C D J, Retter J A, Curtis E A, Hall B V, Llorente García I, Eriksson S, Sauer B E and Hinds E A 2005 *Eur. Phys. J. D* **35** 105

[50] Klank M, Hagedorn O, Holthaus C, Shamonin M and Dötsch H 2003 *NDT & E International* **36** 375

[51] Llorente García I 2008 *Advances in the design and operation of atom chips* Ph.D. thesis Imperial College London

[52] Lu Z T, Corwin K L, Renn M J, Anderson M H, Cornell E A and Wieman C E 1996 *Phys. Rev. Lett.* **77** 3331

[53] Sewell R J, Dingjan J, Baumgärtner F, Llorente-García I, Eriksson S, Hinds E A, Lewis G, Srinivasan P, Moktadir Z, Gollasch C O and Kraft M 2010 *J. Phys. B: At. Mol. Opt. Phys.* **43** 051003

[54] Hall B V, Whitlock S, Anderson R, Hannaford P and Sidorov A I 2007 *Phys. Rev. Lett.* **98** 030402

[55] Fortágh J, Ott H, Kraft S, Günther A and Zimmermann C 2002 *Phys. Rev. A* **66** 041604(R)

[56] Kraft S, Günther A, Ott H, Wharam D, Zimmermann C and Fortágh J 2002 *J. Phys. B: At. Mol. Opt. Phys.* **35** L469

[57] Fortágh J, Ott H, Kraft S, Günther A and Zimmermann C 2003 *Appl. Phys. B* **76** 157

[58] Leanhardt A E, Chikkatur A P, Kielpinski D, Shin Y, Gustavson T L, Ketterle W and Pritchard D E 2002 *Phys. Rev. Lett.* **89** 040401

[59] Leanhardt A E, Shin Y, Chikkatur A P, Kielpinski D, Ketterle W and Pritchard D E 2003 *Phys. Rev. Lett.* **90** 100404

[60] Jones M P A, Vale C J, Sahagun D, Hall B V and Hinds E A 2003 *Phys. Rev. Lett.* **91** 080401

[61] Jones M P A, Vale C J, Sahagun D, Hall B V, Eberlein C C, Sauer B E, Furusawa K, Richardson D and Hinds E A 2004 *J. Phys. B: At. Mol. Opt. Phys.* **37** L15

[62] Vale C J, Upcroft B, Davis M J, Heckenberg N R and Rubinsztein-Dunlop H 2004 *J. Phys. B: At. Mol. Opt. Phys.* **37** 2959

[63] Estève J, Aussibal C, Schumm T, Figl C, Mailly D, Bouchoule I, Westbrook C I and Aspect A 2004 *Phys. Rev. A* **70** 043629

[64] Wang D W, Lukin M D and Demler E 2004 *Phys. Rev. Lett.* **92** 076802

[65] Schumm T, Estève J, Figl C, Trebbia J B, Aussibal C, Nguyen H, Mailly D, Bouchoule I, Westbrook C I and Aspect A 2005 *Eur. Phys. J. D* **32** 171

[66] Krüger P, Andersson L M, Wildermuth S, Hofferberth S, Haller E, Aigner S, Groth S, Bar-Joseph I and Schmiedmayer J 2007 *Phys. Rev. A* **76** 063621

[67] Moktadir Z, Darquié B, Kraft M and Hinds E A 2007 *Journal of Modern Optics* **54** 2149

[68] Whitlock S, Hall B V, Roach T, Anderson R, Volk M, Hannaford P and Sidorov A I 2007 *Phys. Rev. A* **75** 043602

[69] Sinclair C D J 2005 *Bose-Einstein Condensation in Microtraps on Videotape* Ph.D. thesis Imperial College London

[70] Trebbia J B, Garrido Alzar C L, Cornelussen R, Westbrook C I and Bouchoule I 2007 *Phys. Rev. Lett.* **98** 263201

[71] Bouchoule I, Trebbia J B and Garrido Alzar C L 2008 *Phys. Rev. A* **77** 023624

[72] Petrich W, Anderson M H, Ensher J R and Cornell E A 1995 *Phys. Rev. Lett.* **74** 3352

[73] Reichel J and Thywissen J H 2004 *J. Phys. IV France* **116** 265

[74] Dekker N H, Lee C S, Lorent V, Thywissen J H, Smith S P, Drndíc M, Westervelt R M and Prentiss M 2000 *Phys. Rev. Lett.* **84** 1124

[75] Hänsel W, Reichel J, Hommelhoff P and Hänsch T W 2001 *Phys. Rev. Lett.* **86** 608

[76] Hänsel W, Hommelhoff P, Hänsch T W and Reichel J 2001 *Nature* **413** 498

[77] Hommelhoff P, Hänsel W, Steinmetz T, Hänsch T W and Reichel J 2005 *New Journal of Physics* **7** 063621

[78] Long R, Rom T, Hänsel W, Hänsch T W and Reichel J 2005 *Eur. Phys. J. D* **35** 125

[79] Günther A, Kemmler M, Kraft S, Vale C J, Zimmermann C and Fortágh J 2005 *Phys. Rev. A* **71** 063619

[80] Whitlock S, Gerritsma R, Fernholz T and Spreeuw R J C 2009 *New J. Phys.* **11** 023021

[81] Rosenbusch P, Hall B V, Hughes I G, Saba C V and Hinds E A 2000 *Phys. Rev. A* **61** 031404(R)